Shape Modeling and Atlas-Based Segmentation for Identification of Lower Leg Tissues in pQCT

S. Makrogiannis[1], *A. Okorie*[1], *T. Biswas*[1] *and L. Ferrucci*[2]

[1]Division of Physics, Engineering, Mathematics and Computer Science, Delaware State University, Dover, DE, USA
[2]National Institute on Aging, National Institutes of Health, Baltimore, MD, USA
smakrogiannis@desu.edu

***Abstract*—In this work, we introduce an atlas-based segmentation method for lower leg tissues at 4%, 38%, and 66% tibial length. Our goal is to model the shape of the lower leg tissue types and to identify hard and soft tissues in an automated way. In our methodology, we implemented B-spline based free form deformation (FFD), and symmetric diffeomorphic demons (SDD) deformable models for nonlinear registration, and compared their performances for atlas-based segmentation accuracy on our pQCT data. Overall, we concluded that atlas-based segmentation is a promising technique, especially in the presence of noise and other types of image degradation. We also observed that the diffeomorphic demons algorithm may produce more accurate deformation fields than FFD. On the other hand, FFD produced smoother deformations than SDD. Quantitative analysis using the Dice similarity coefficient (DSC), showed that FFD was slightly better than SDD in identification of the trabecular bone tissue in 4% tibia. At 38% tibial length, SDD produced consistently higher DSC values than FFD, while at 66% tibia, FFD produced slightly higher segmentation accuracy.**

I. Introduction

In the biomedical image analysis domain, segmentation refers to the process of delineation and identification of objects or tissues in images. While there are many image segmentation methods, yet it is a problem-specific or a domain-specific task, and it depends on the image data, the objects imaged, and the type of desired output information. Radiological imaging techniques are subject to imaging artifacts such as noise, beam hardening, ring artifacts, partial voluming, and noise. Traditional methods for delineating biomedical images involve semi-manual supervised operations, which are slow, subject to error, and their accuracy depends on the performance of the expert [1]. Atlas-based segmentation offers an automated, fast, robust to noise and accurate solution to diverse biomedical image segmentation problems.

An *atlas* is an image that incorporates the locations and shapes of anatomical structures, and spatial relationships between them [2]. It provides a complete description of neighborhood relationships between several different (anatomical) structures. The literature in this field includes numerous methods and significant applications such as tissue identification, computational anatomy, and surgical planning [1], [3], [2], [4], [5], [6].

In this paper, we introduce our atlas-based tissue segmentation method applied to peripheral Quantitative Computed Tomography (pQCT) scans of the lower leg at anatomical sites corresponding to 4%, 38% and 66% of the tibial length, (see Figure 1 for an example). Our goal is to model the shape of the hard and soft tissue regions and perform fully automated tissue delineation. The tissue types that we wish to quantify are summarized in Table I.

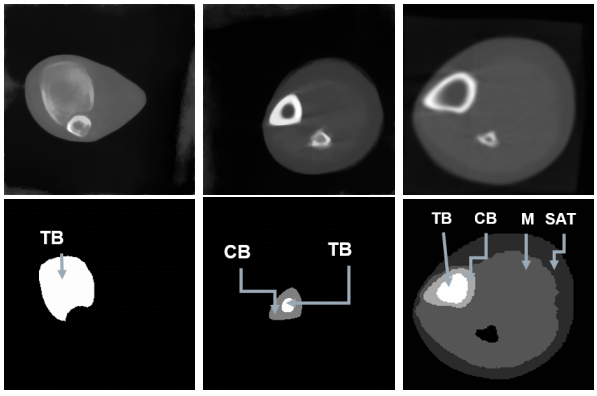

Figure 1. Statistical atlases for 4%, 38% and 66% tibial length in the lower leg (top, left to right), and their corresponding labels (bottom, left to right). TB-Trabecular Bone, CB-Cortical Bone, M-Muscles and SAT-Subcutaneous Adipose Tissue. We generated the atlases using the procedure in Section II-B. We delineated the tissue labels using a semi-manual workflow.

Table I
Tissues to quantify in the different anatomical sites.

Anatomical Site	Tissues to quantify
4%	Trabecular Bone
38%	Cortical Bone, Trabecular Bone
66%	Cortical Bone, Trabecular Bone, SAT, Muscle

The method includes two major stages: atlas generation and segmentation. In each of these stages, we employed both linear and nonlinear registration techniques. The linear registration stage, which we modeled by affine transformation, is used to address global misalignments between images. In the nonlinear registration stage, we employed two deformable models, namely, *free-form deformable registration using B-splines* [7], and *symmetric diffeomorphic demons* [8].

We validated and compared the performance of the deformable registration methods. For each of the deformable models, we performed experiments using the calculated statistical atlas [3]. Our results showed that our atlas-based system produced good rates of segmentation accuracy even for data with visible image quality degradation. In addition, symmetric diffeomorphic demons may produce slightly more accurate delineations than B-spline-based FFD.

The remaining sections of the paper are structured as follows: in Section II, we first describe the linear and deformable registration techniques that we employed. Next, we explain the statistical-average atlas generation and our atlas-based segmentation technique. In Section III we describe our experiments and discuss the results. Lastly, Section IV concludes this work.

II. Atlas-based Tissue Identification

Two fundamental stages in an atlas-based segmentation framework are i) atlas generation and ii) segmentation, or label propagation. Image registration is a key process in both stages.

A. Registration

Let I and R be the input and reference images, with their respective spatial domains Ω_I and Ω_R. Sotiras et al. [6], defined the goal of image registration in biomedical imaging domain in terms of finding an optimal transformation $\tau : \Omega_I \rightarrow \Omega_R$ that maps $\mathbf{x} \in \Omega_I$ to $\tau(\mathbf{x}) \in \Omega_R$, and optimizes an energy of the form

$$E(\tau) = \lambda_s s(R, I \circ \tau) + \lambda_r r(\tau). \tag{1}$$

In equation (1), τ is the deformation field and is defined in [6] as a sum of the displacement field $\mathbf{u}$ and the coordinate vector $\mathbf{x}$

$$\tau(\mathbf{x}) = \mathbf{u}(\mathbf{x}) + \mathbf{x}. \tag{2}$$

The deformation field τ warps coordinates of the reference space to the input space. The function $s(\cdot,\cdot)$ is the *similarity measure*. It is used to quantify the level of alignment between R and I, and also measures the correctness of the mapping τ, between I and R. The *regularization term* r encodes the desired properties of τ. It also serves as the smoothing term or filter for τ. The parameters, λ_s and λ_r denote the weights of the residual and regularization terms respectively.

In our atlas-based segmentation system, we employ both linear and nonlinear registration models, to account for global as well as local misalignments.

Linear Registration

We implement a *linear model* τ_L, to capture the global motion of the lower leg. We model the linear registration using affine transforms. We utilize the Mattes' Mutual Information similarity metric and a regular step gradient descent optimizer.

Nonlinear Registration

The nonlinear (deformable model, $\tau := \tau_{NL}$) registration is used to address inter-individual variability in shapes of anatomical structures.

We employ multi-grid FFD and Symmetric Diffeomorphic demons on log-domain (SDD) techniques.

1) Multi-Grid FFD: Rueckert et. al [7] modeled nonlinear deformations using B-spline based free-form deformations. Because our method is applied to 2D images, we present the 2D version of FFD. Given the spatial domain, $\Omega = \{\mathbf{x} = (x, y) | 0 \leq x < X, 0 \leq y < Y\}$ of an image, let Φ denote an $n_x \times n_y$ mesh of control points $\phi_{i,j}$ with uniform spacing δ. Then, the FFD (displacement field τ) [7] can be written as the 2-D tensor product of 1-D cubic FFD

$$\tau(\mathbf{x}) = \sum_{l=0}^{3} \sum_{m=0}^{3} B_l(u) B_m(v) \phi_{i+l, j+m} \tag{3}$$

where $i = \lfloor x/n_x \rfloor - 1, j = \lfloor y/n_y \rfloor - 1, u = x/n_x - \lfloor x/n_x \rfloor, v = y/n_y - \lfloor y/n_y \rfloor$, and B_l represents the lth basis function of the B-spline.

$$\begin{aligned} B_0(u) &= (1-u)^3/6 \\ B_1(u) &= (3u^3 - 6u^2 + 4)/6 \\ B_2(u) &= (-3u^3 + 3u^2 + 3u + 1)/6 \\ B_3(u) &= u^3/6. \end{aligned}$$

To ensure that τ produces a smooth transformation, we used the bending energy of a thin-plate of metal r as the regularization term given by

$$\begin{aligned} r(\tau) = \frac{1}{|\Omega|} \int_0^X \int_0^Y \left[\left(\frac{\partial^2 \tau}{\partial x^2} \right)^2 + \left(\frac{\partial^2 \tau}{\partial y^2} \right)^2 \right. \\ \left. + 2 \left(\frac{\partial^2 \tau}{\partial xy} \right)^2 \right] dxdy, \end{aligned} \tag{4}$$

where $|\Omega|$ is the area of the image domain.

The normalized mutual information, given in Equation (5)

$$s(A, B) = \frac{H(A) + H(B)}{H(A, B)} \tag{5}$$

served as the similarity measure to avoid any dependence on the degree of image overlap. More information on the B-spline based FFD and the optimization stages can be found in [7]. An advantage of B-spline FFD is that it can produce smooth deformations with a moderate number of parameters, nevertheless, it may not preserve the topology very well.

2) Diffeomorphic Demons: In the method described in [9], the demons algorithm was employed for minimization of the energy functional given in Equation (1), by introducing a variable c [10] to approximate the error in the correspondence between image pixels. Thus the global energy in Equation (1) is modified as

$$E(c, \tau) = \frac{1}{\lambda_s^2} s(R, I, c) + \frac{1}{\lambda_h^2} d(\tau, c)^2 + \frac{1}{\lambda^2} r(\tau) \tag{6}$$

where the similarity criterion $s(\cdot,\cdot,\cdot)$, is given by

$$s(R, I, c) = \frac{1}{2} \|R - I \circ c\|^2 = \frac{1}{2|\Omega_{\mathbf{p}}|} \sum_{\mathbf{x} \in \Omega_{\mathbf{x}}} |R(\mathbf{x}) - I(c(\mathbf{x}))|^2, \tag{7}$$

and λ accounts for spatial uncertainty on the correspondences. Also, $d(\tau, c) = \|c - \tau\|$ and $r(\tau) = \|\nabla \tau\|^2$.

Fluid-like constraints may be applied by modifying the regularization term [10]. $\Omega_{\mathbf{p}}$ is the region of the intersection between R and $I \circ \tau$.

The minimization process was based on additive iterations of the form $\tau \leftarrow \tau + \mathbf{u}$ using classical descent methods. By introducing the auxiliary variable c, the optimization scheme alternates over c and τ thereby simplifying and increasing the efficiency of the complex minimization steps [9].

Application of classical Newton's method on the energy function of (6) yields the following update equation

$$\mathbf{u}(\mathbf{x}) = -\frac{R(\mathbf{x}) - I \circ \tau(\mathbf{x})}{\|J^p\|^2 + \frac{\sigma_i^2(\mathbf{x})}{\sigma_x^2}} J^{\mathbf{x}\top} \tag{8}$$

where λ_h controls the maximum step length: $\|\mathbf{u}(\mathbf{x})\| \leq \lambda_h/2$. To make the transformation diffeomorphic, τ is replaced with the composition of τ and exponential $\exp(\mathbf{u})$, i.e., $\tau \leftarrow \tau \circ \exp(\mathbf{u})$, thus exploring the Lie group structure on diffeomorphisms.

A log-domain representation of the complete spatial transformation is achieved by defining τ as the exponential function of the smooth vector field, $\tau := \exp(v)$ [8]. To accomplish this, the authors of [8] used Baker-Campbell-Hausdorff (BCH) approximations to seek a smooth velocity field $Z(v, \varepsilon\mathbf{u})$, such that $\exp(Z(v, \varepsilon\mathbf{u}) \approx \exp(v) \circ \exp(\varepsilon\mathbf{u})$, where ε is a weight parameter.

Log-Domain Diffeomorphic Demons: Using the BCH approximations, the field update $\tau \leftarrow \tau \circ \exp(\mathbf{u})$ used in the diffeomorphic demons could be converted into a log-domain update $v \leftarrow Z_X(v, \mathbf{u})$, provided that the current transformation τ can be expressed as an exponential $\tau = \exp(v)$. Gaussian smoothing is performed directly in the log domain in order to keep the field consistent with the log-domain representation, while maintaining the simplicity of the demons algorithm. The log-domain framework can simply be linked to (1) by defining $d(c, \tau) = \| \log(\tau^{-1} \circ c\|$ and $r(\tau) = \|\nabla \log(\tau)\|^2$.

Symmetric Extension: In the log-domain, the inverse spatial transform, τ^{-1} of $\tau = \exp(v)$ that is $\tau^{-1} := \exp(-v)$, can be obtained efficiently by backward computation. Therefore, a symmetric transformation can be derived from a nonsymmetric one by making the global energy symmetric, i.e.,

$$\tau_{opt} = \arg\min_{\tau} \left(E_{sym} := E(R, I \circ \tau) + E\left(I, R \circ \tau^{-1}\right)\right) \tag{9}$$

The authors in [8], developed a technique to minimize a symmetric global energy that is formulated as a constrained equation using two diffeomorphisms

$$[\tau_{opt}, \tau_{opt}^{-1}] = \arg\min_{[\tau, \tau^{-1}]} E_{sym}$$

An unconstrained optimization step was used on the pair $[\tau, \rho]$ and then the new transformations are projected onto the space of symmetric transformations $\{[\tau, \rho] | \rho = \tau^{-1}\}$.

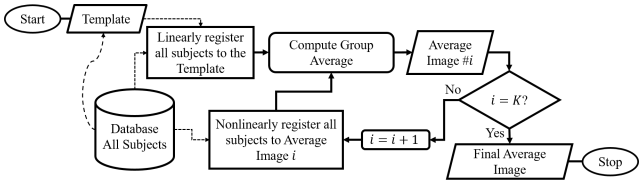

Figure 2. Statistical average atlas generation algorithm.

B. Average Atlas Generation

We generate the statistical atlases by iteratively calculating group averages over registered images. The average atlas gives a statistical description of all subjects by means of the group average and deviation. In this approach, one subject is chosen from a data set, as the reference. Then, we linearly register all subjects to the selected reference and compute the group average. In the second iteration $i = 2$, the group average image from linear registration is chosen as reference, then all subjects are registered to the new reference, nonlinearly and the average is computed. For iterations $i \geq 3$, the nonlinearly registered average image from the preceding iteration is set as the reference, then all subjects are again nonlinearly registered to the chosen reference, and the average is computed average at each iteration. The process is continued until the final iteration $i = K$. In the generation of statistical atlases, we used $K = 10$ iterations. Figure 2 outlines the statistical atlas calculation algorithm.

A sequence of transformations $\tau_i^{(n)}$, where $n = 0, 1, 2, \ldots, N$ is the nth image and $i = 0, 1, \ldots, K$ is the ith iteration, is generated with the property that for each iteration i, the transformation $\tau_i^{(n+1)}$ and the preceding transformation $\tau_i^{(n)}$ differ only by a small amount of deformation [3]. After generating the statistical atlas image, we manually labeled the tissues. The first row in Figures 4, 5 and 6 displays the atlas image and atlas label map for 4%, 38% and 66% of the tibia length, respectively.

C. Atlas-based Segmentation

We employ atlas-based segmentation to segment all subjects using the atlas image and the corresponding label image (segmented atlas). The process can be divided into two parts: 1) establishment of spatial correspondences between the atlas and the subject, 2) propagation of labels [1]. The process is described in Figure 3.

1) Spatial Correspondence: In the registration process, the atlas A is the input image, while the individual subjects are the reference images. First, we model a rigid transformation, τ_L by linearly registering the atlas intensity image to the subject. Then we apply τ_L to the coordinate space of atlas intensity image A to obtain linearly registered atlas image $\tau_L(A)$. Secondly, we estimate the deformable model τ_{NL}, by a nonlinear registration of $\tau_L(A)$ to the subject image. Then the nonlinear transformation τ_{NL} is used to warp the coordinate space of the linearly registered atlas pixel image to the subject space, to obtain $\tau_{NL} \circ \tau_L(A) = \tau_{NL}(\tau_L(A))$. If the above process is successful, we observe

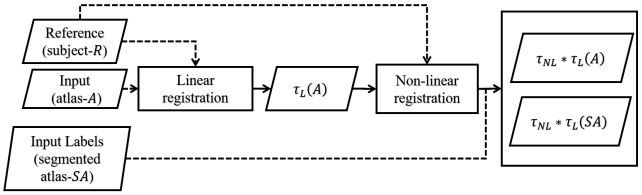

Figure 3. Atlas-based segmentation.

that the deformed atlas image is similar in structure and spatial location to the original subject image. We show examples of $\tau_L(A)$ and $\tau_{NL}(\tau_L(A))$ for 4%, 38% and 66% tibia sites in Figures 4, 5 and 6 respectively.

2) Label Propagation: After we have established the spatial correspondence between SA and A using the linear and nonlinear deformations τ_L and τ_{NL}, the next step is to assign labels from the atlas to the subject space. We apply the estimated deformation $\tau_{NL} \circ \tau_L$ to the segmented (labeled) atlas to propagate labels to the subject domain. The segmentation results are defined as $\tau_{NL}(\tau_L(SA))$ (see results in Figures 4, 5 and 6, corresponding to tissue identification of 4%, 38% and 66% of tibia).

III. Results and Discussion

In this section, we discuss our datasets, the purpose of our experiments, and the results we obtained.

A. Dataset

Our dataset consists of randomly selected pQCT scans from three different anatomical sites of the lower leg, namely 4%, 38%, and 66% tibia. The data were obtained from the InCHIANTI study that is a population-based cohort study that was performed in two Italian towns in the Chianti region (Greve and Bagno). The test dataset is a random sample of participants aged 65 years or older and a group of men and women randomly selected for each decade between 20 and 70 years of age that was provided by Lauretani et al in [11]. The InChianti study excluded participants who were receiving medication, or had conditions affecting the bone metabolism. The experimental procedures involving human subjects were approved by the Institutional Review Board of the institution that provided the data. The clinical trial design and data collection methods of InChianti were described in more detail in [12] and [13].

B. Experiments

We tested our atlas-based segmentation with 30 different subjects at 4% tibia, 26 subjects at 38% tibia and 20 subjects at 66% tibia. Reference label data, consisting of manually segmented images were also provided for all images in the three anatomical sites, to be used for validation of segmentation accuracy.

Our experiments were focused on shape modeling and identification of lower leg (tibia) tissues in pQCT using atlas-based segmentation. A list of the three different anatomical sites and the corresponding tissues to identify is given in Table I. We divided our experiments into two parts, 1) using free-form deformations, and 2) using diffeomorphic demons. The segmentation accuracy for each tissue in each of the anatomical sites was validated using the Dice similarity coefficient (DSC) given by $\text{DSC}(R,S) = \frac{2|R \cap S|}{|R|+|S|}$, where R stands for a tissue label in the reference image and S represents the corresponding tissue label in the segmented image.

C. Qualitative Results

Typical examples of the result of atlas-based segmentation, and identification of tissues in the 4%, 38% and 66% anatomical sites of the lower leg, using FFD and diffeomorphic demons, are shown in Figures 4, 5 and 6. In these examples, it appears that the FFD method yielded more accurate segmentation than SDD for 4% of the tibial length, but at 38% and 66% tibial length, we observe that the results of SDD seem to produce more accurate segmentation. In the 38% and 66% sites, we observe that the tissues (cortical and trabecular bones) in the results of the FFD method still maintained the shape of the atlas to some extent, whereas the SDD results tend more to assume the shape of tissues in the subject image. Also in the 66% site results, the space between the SAT and muscle tissues tends to be narrower for the SDD algorithm, as it appears in the input image, than it does appear in the result obtained with FFD.

Although visual inspection provides insight into the performance of our methodology, yet we need quantitative evaluation to make objective conclusions. The quantitative analysis of our method follows in the next subsection.

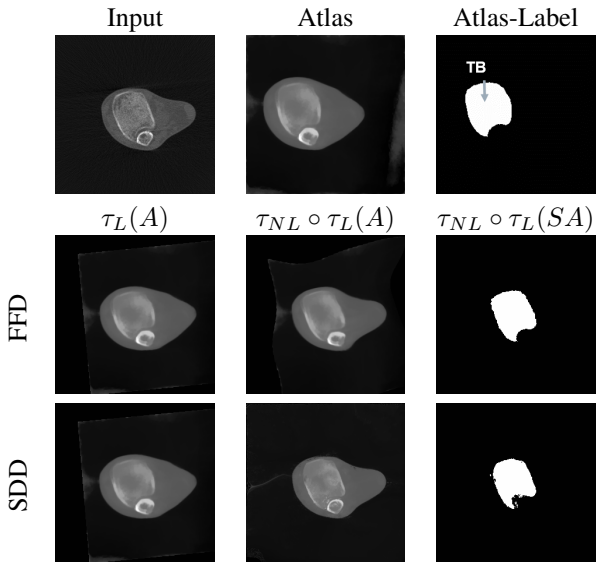

Figure 4. Example of individual stages of atlas-based segmentation of 4% tibia site using FFD (middle row) and SDD (bottom row).

D. Quantitative Results

We segmented all subjects in each dataset using FFD and SDD and calculated the DSC of the individual tissue types for each method.

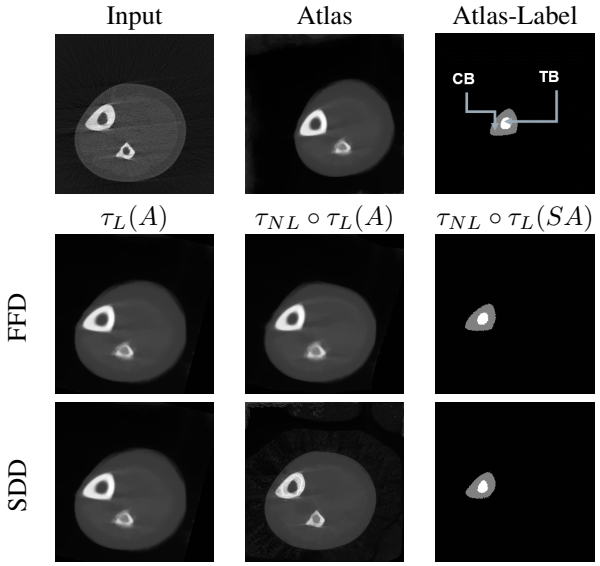

Figure 5. Example of individual stages of atlas-based segmentation of 38% tibia site using FFD (middle row) and SDD (bottom row).

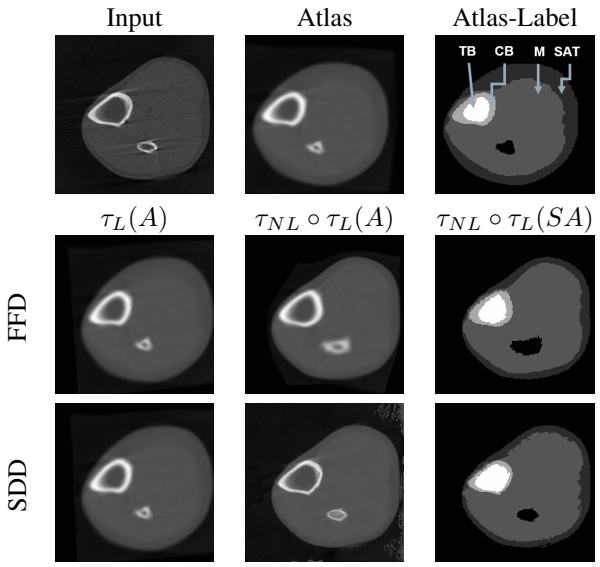

Figure 6. Example of individual stages of atlas-based segmentation of 66% tibia site using FFD (middle row) and SDD (bottom row).

1) 4% tibia site: Here we are interested in identifying the trabecular bone. We segmented all 30 scans using FFD and SDD, and calculated DSC the trabecular bone (TB) tissue for each method. We used box plots to represent the range of DSC values of the trabecular bones of all 30 subjects for each method in Figure 7. We display the DSC for FFD and SDD on the left and on the right side respectively. This plot shows that FFD produced better segmentation accuracy than the SDD, as the lowest value is about 90%. We also calculated the average DSC over all subjects that showed that the DSC of FFD ($\sim$95.6%) is greater than SDD ($\sim$ 93.7%).

2) 38% tibia site: We performed experiments with atlas-based segmentation on 26 scans of the 38% tibia site using FFD and SDD. The tissues of interest are the cortical

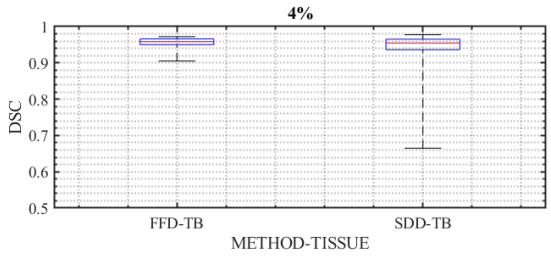

Figure 7. Box plots of DSC values of 4% segmentation results for all subjects, each tissue and each method. The red horizontal line within the box is the median over all subjects, the vertical lines show the range of values, the box shows the 25^{th} and the 75^{th} percentiles of the respective distributions.

bone (CB) and the trabecular bone (TB). We calculated the DSC for each tissue between segmentation results and the reference label maps, and compared the performance of the two deformable models. The DSCs for all subjects, each tissue, and each method are represented by the box plot in Figure 8. We observe that for both tissues, the DSC values for SDD are higher than that of FFD. The range of values for SDD is more compact and on the upper values than FFD which shows a wider spread and has values that are less than 65%. The average DSC values are summarized in Table II. We observe that the diffeomorphic demons (SDD) algorithm performed better than the free-form deformation (FFD) with B-splines.

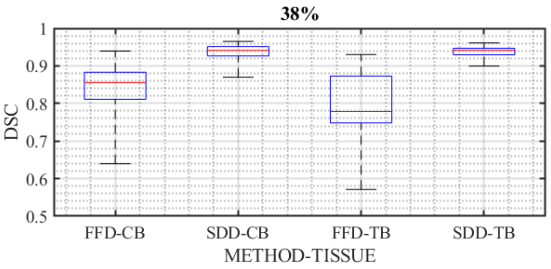

Figure 8. Box plots of DSC values of 38% segmentation results for segmented subjects, each tissue and each method. [See Figure 7 for details about box plots].

Table II
DSC VALUES ($\mu \pm \sigma$) OF TISSUE IDENTIFICATION IN 38% TIBIA

Method	Cortical Bone	Trabecular Bone
FFD	84.8 ± 7.6	79.7 ± 9.7
SDD	93.9 ± 2.2	93.6 ± 2.1

3) 66% tibia site: 20 scans at the 66% tibia site were segmented in this experiment. The tissues of interest are the subcutaneous fat (SAT), muscle (M), cortical bone (CB), and trabecular bone (TB). The box plots in Figure 9, illustrate the performance of each method in the identification of the aforementioned tissues over all the subjects. We observe that, apart from the SAT, the maximum DSC value obtained using SDD is always greater than that of FFD, in the remaining three tissues. Also, the minimum

values for SDD are always greater than FFD. Although the median mark for FFD is greater in SAT, CB, and TB than SDD, yet the range of values for the individual tissues is more compact for SDD than FFD. The DSC values are summarized in Table III. The results show that SDD and FFD produce close expected values for DSC.

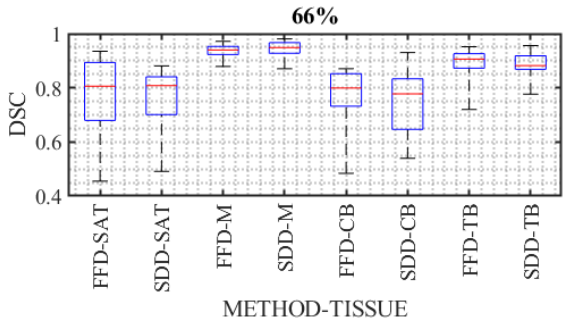

Figure 9. Box plots of DSC values of 66% segmentation results for segmented subjects, each tissue and each method. [See Figure 7 for details about box plots].

Table III
DSC VALUES ($\mu \pm \sigma$) OF TISSUE IDENTIFICATION IN 66% TIBIA

Method	SAT	Muscle	Cortical Bone	Trabecular Bone
FFD	77.7 ± 13.7	93.8 ± 2.4	76.1 ± 11.8	88.9 ± 5.6
SDD	75.2 ± 13.1	94.3 ± 3.0	75.3 ± 10.7	88.1 ± 5.2

IV. CONCLUSION

In this work, we employed atlas-based segmentation for shape modeling and identification of tissue objects in pQCT. We considered three datasets corresponding to the three tibia sites of the lower leg, namely at 4%, 38% and 66% of the tibial length. We generated a statistical atlas by an iterative shape averaging algorithm, for each anatomical site, to use for segmentation of the subjects in each dataset. In the registration part of our methodology, we compared the performance of two nonlinear deformable models, namely: free-form deformations (FFD) using B-splines and diffeomorphic demons (SDD). We evaluated the accuracy of tissue identification at three anatomical sites, using the Dice similarity coefficient (DSC). Our results showed that the diffeomorphic demons approach has slightly better potential to identify the shape of tissues in pQCT data than FFD. Furthermore, both methods showed robustness to image degradation and noise. Although SDD deformations may be slightly more accurate, they may be affected by noise, because SDD is a variational intensity-based registration technique. On the other hand, the FFD deformations are smooth i.e., robust to noise, but may yield slightly lower delineation accuracy.

ACKNOWLEDGMENT

This work was partially supported by the National Institute of General Medical Sciences of the National Institutes of Health (NIH) under Award Number SC3GM113754 and by the Intramural Research Program of NIA, NIH.

REFERENCES

[1] J. E. Iglesias and M. R. Sabuncu, "Multi-atlas segmentation of biomedical images: A survey," *Medical image analysis*, vol. 24, no. 1, pp. 205–219, 2015.

[2] T. Rohlfing, R. Brandt, R. Menzel, D. B. Russakoff, and C. R. Maurer, *The Handbook of Medical Image Analysis-Volume III: Registration Models*. New York, NY: Kluwer Academic/Plenum Publishers, 2005, ch. Quo Vadis, Atlas-Based Segmentation?, pp. 435–486.

[3] T. Rohlfing, R. Brandt, C. R. Maurer, and R. Menzel, "Bee brains, b-splines and computational democracy: Generating an average shape atlas," in *Proceedings IEEE Workshop on Mathematical Methods in Biomedical Image Analysis (MMBIA 2001)*. IEEE, 2001, pp. 187–194.

[4] T. R. Langerak, U. A. van der Heide, A. N. Kotte, M. A. Viergever, M. Van Vulpen, J. P. Pluim *et al.*, "Label fusion in atlas-based segmentation using a selective and iterative method for performance level estimation (simple)," *IEEE transactions on medical imaging*, vol. 29, no. 12, pp. 2000–2008, 2010.

[5] Dinggang Shen and C. Davatzikos, "Hammer: Hierarchical attribute matching mechanism for elastic registration," *IEEE Transactions on Medical Imaging*, vol. 21, no. 11, pp. 1421–1439, Nov. 2002.

[6] A. Sotiras, C. Davatzikos, and N. Paragios, "Deformable medical image registration: A survey," *IEEE Transactions on Medical Imaging*, vol. 32, no. 7, pp. 1153–1190, Jul. 2013.

[7] D. Rueckert, L. I. Sonoda, C. Hayes, D. L. G. Hill, M. O. Leach, and D. J. Hawkes, "Nonrigid registration using free-form deformations: Application to breast mr images," *IEEE Transactions on Medical Imaging*, vol. 18, no. 8, pp. 712–721, Aug. 1999.

[8] T. Vercauteren, X. Pennec, A. Perchant, and N. Ayache, "Symmetric log-domain diffeomorphic registration: A demons-based approach," in *International conference on medical image computing and computer-assisted intervention*. Springer, 2008, pp. 754–761.

[9] T. Vercauteren, X. Pennec, A. Perchant, and N. Ayache, "Non-parametric diffeomorphic image registration with the demons algorithm," in *International Conference on Medical Image Computing and Computer-Assisted Intervention*. Springer, 2007, pp. 319–326.

[10] P. Cachier, E. Bardinet, D. Dormont, X. Pennec, and N. Ayache, "Iconic feature based nonrigid registration: The pasha algorithm," *Computer vision and image understanding*, vol. 89, no. 2-3, pp. 272–298, 2003.

[11] F. Lauretani, S. Bandinelli, M. E. Griswold, M. Maggio, R. Semba, J. M. Guralnik, and L. Ferrucci, "Longitudinal changes in bmd and bone geometry in a population-based study," *Journal of Bone and Mineral Research*, vol. 23, no. 3, pp. 400–408, 2008.

[12] L. Ferrucci, S. Bandinelli, E. Benvenuti, A. Di Iorio, C. Macchi, T. B. Harris, and J. M. Guralnik, "Subsystems contributing to the decline in ability to walk: Bridging the gap between epidemiology and geriatric practice in the inchianti study," *Journal of the American Geriatrics Society*, vol. 48, no. 12, pp. 1618–1625, 2000.

[13] S. Makrogiannis, F. Boukari, and L. Ferrucci, "Automated skeletal tissue quantification in the lower leg using peripheral quantitative computed tomography," *Physiological measurement*, vol. 39, no. 3, p. 035011, 2018.